

# Putting People in their Place: Monocular Regression of 3D People in Depth

Yu Sun<sup>1\*</sup> Wu Liu<sup>2</sup> Qian Bao<sup>2</sup> Yili Fu<sup>1</sup> Tao Mei<sup>2</sup> Michael J. Black<sup>3</sup>  
<sup>1</sup>Harbin Institute of Technology, Harbin, China <sup>2</sup>JD AI Research, Beijing, China  
<sup>3</sup>Max Planck Institute for Intelligent Systems, Tübingen, Germany  
 yusun@stu.hit.edu.cn, liuwu@live.cn, baoqian@jd.com, meylfu@hit.edu.cn  
 tmei@live.com, black@tuebingen.mpg.de

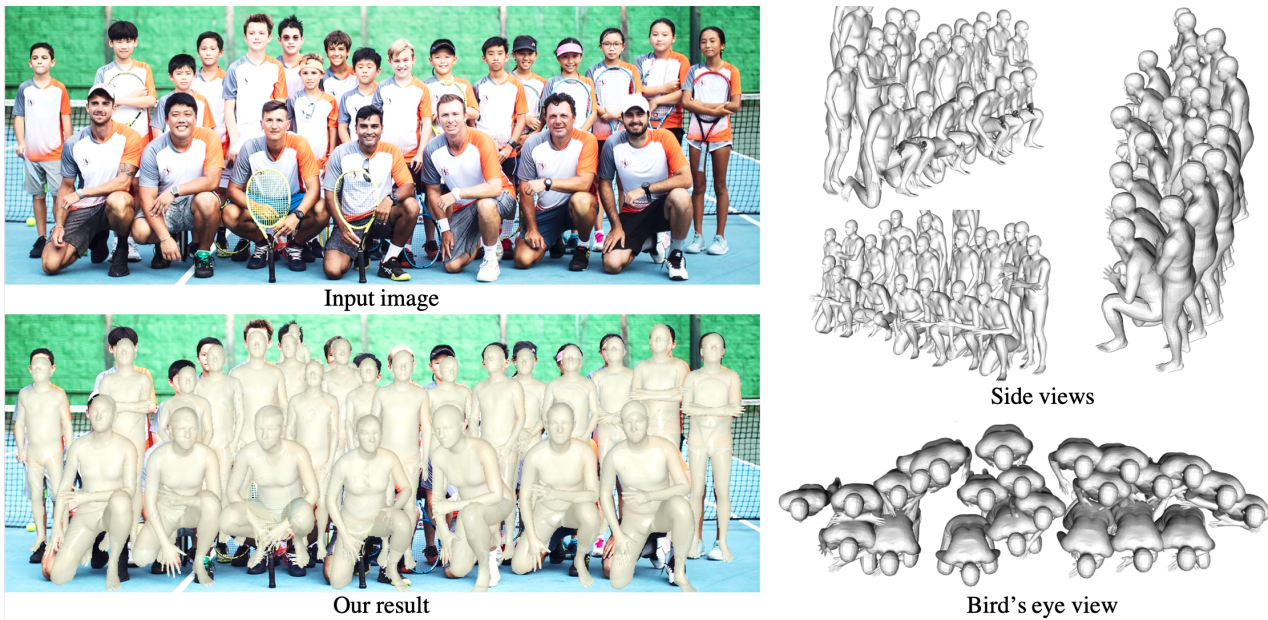


Figure 1. **Monocular reconstruction of multiple 3D people with coherent depth reasoning.** We introduce BEV, a monocular one-stage method with an efficient new “bird’s-eye-view” representation, which enables the network to explicitly reason about people in 3D.

## Abstract

Given an image with multiple people, our goal is to directly regress the pose and shape of all the people as well as their relative depth. Inferring the depth of a person in an image, however, is fundamentally ambiguous without knowing their height. This is particularly problematic when the scene contains people of very different sizes, e.g. from infants to adults. To solve this, we need several things. First, we develop a novel method to infer the poses and depth of multiple people in a single image. While previous work that estimates multiple people does so by reasoning in the image plane, our method, called BEV, adds an additional imaginary Bird’s-Eye-View representation to explicitly reason about depth. BEV reasons simultaneously about body

centers in the image and in depth and, by combing these, estimates 3D body position. Unlike prior work, BEV is a single-shot method that is end-to-end differentiable. Second, height varies with age, making it impossible to resolve depth without also estimating the age of people in the image. To do so, we exploit a 3D body model space that lets BEV infer shapes from infants to adults. Third, to train BEV, we need a new dataset. Specifically, we create a “Relative Human” (RH) dataset that includes age labels and relative depth relationships between the people in the images. Extensive experiments on RH and AGORA demonstrate the effectiveness of the model and training scheme. BEV outperforms existing methods on depth reasoning, child shape estimation, and robustness to occlusion. The code and dataset will be released for research purposes.

\*This work was done when Yu Sun was an intern at JD AI Research.

## 1. Introduction

In this article, we focus on simultaneously estimating the 3D pose and shape of all people in an RGB image along with their relative depth. There has been rapid progress on regressing the 3D pose and shape of individual (cropped) people [3, 13–16, 22, 26, 31, 37, 38] as well as the direct regression of groups [10, 30]. Neither class of methods explicitly reasons about the depth of people in the scene. Such depth reasoning is critical to enable a deeper understanding of the scene and the multi-person interactions within it. To address this, we propose a unified method that jointly regresses multiple people and their relative depth relations in one shot from an RGB image.

While previous multi-person methods perform well in constrained experimental settings, they struggle with severe occlusion, diverse body size and appearance, the ambiguity of monocular depth, and in-the-wild cases [10, 21, 34, 39, 41]. These challenges lead to unsatisfactory performance in crowded scenes, including detection misses, similar predictions for overlapping people, and all predictions having a similar height. We observe two inter-related limitations that result in these failures. First, the architecture of the regression networks is closely tied to the 2D image, while the people actually inhabit 3D space. We address this with a new architecture that reasons in 3D. Second, depth estimation is fundamentally ambiguous due to the unknown height of the people in the image and it is difficult to obtain training data of images with ground-truth height and depth. To address this, we present a new dataset and novel losses that allow training without having metric depth.

We observe that crowded scenes contain rich information about the relative relationships between people, which can be exploited for both training and validation of depth reasoning. However, current methods lack sufficiently powerful representations to learn from these cases. A few learning-based methods have been proposed for depth reasoning of predicted body meshes [10, 39] or 3D poses [21, 34, 41]. Unfortunately, they all reason about depth via 2D representations, such as RoI-aligned features [10, 21], a 2D depth map [34, 41], or multi-scale 2D center maps [39]. These regression-based 2D representations have inherent drawbacks for representing the 3D world. The lack of an explicit 3D representation in the networks makes it challenging for these methods to deal with crowded scenes in which people overlap at different depths. Therefore, we argue that an explicit 3D representation is needed.

To achieve this, we develop BEV (for Bird’s Eye View), a unified one-stage method for monocular reconstruction and depth reasoning of multiple 3D people. We take inspiration from ROMP [30], a one-stage, multi-person, regression method that directly estimates multiple 2D front-view maps for 2D human detection, positioning, and mesh parameter regression without depth reasoning. With ROMP, the net-

work can only reason about the 2D location of people in the image plane. To go beyond this, we need to enable the network to efficiently reason about depth as well. To that end, we introduce a new *imaginary* 2D “bird’s-eye-view” map that represents the likely centers of bodies in depth. To be clear, BEV takes only a single 2D image; the overhead view is inferred, not observed. BEV uses a powerful and efficient localization pipeline, performing bird’s-eye-view-based coarse detection and fine localization in parallel. We employ the 2D heatmaps for coarse detection from both the front (image) and bird’s eye views. BEV combines these heatmaps to obtain a 3D heatmap, as illustrated in Fig. 2. By learning the front and the bird’s-eye view together, BEV explicitly models how people appear in images and in depth. This enables BEV to learn from available 2D and 3D annotations. BEV also uses a novel 3D offset map to refine the initial coarse detections. From these coarse and fine maps, we obtain the 3D translation of all people in the scene. BEV transforms these predictions from the latent 3D center-map space to an explicit camera-centric 3D space. Given these 3D translation predictions, BEV samples the pose features of all the people from a predicted mesh feature map and regresses the final SMPL [19] pose parameters. Distinguishing people at different depths enables BEV to estimate multiple people even with severe occlusion as illustrated in Fig. 1.

Even with a powerful 3D representation, we need an appropriate training scheme to ensure generalization. The main reason is that without knowing subject height, we lack effective constraints to alleviate the depth/height ambiguity under perspective projection. In particular, height varies with age, making it impossible to resolve depth without also estimating the age of people in the image. The ambiguity causes incorrect depth estimates for children and infants, limiting the generalization of existing methods. Unfortunately, existing 3D datasets with multiple people have limited diversity in height and age, so they cannot be used to improve or evaluate generalization.

Since collecting ground-truth 3D data in the wild is difficult, we instead train BEV using cost-effective weak labels of in-the-wild images. Specifically, we collect a dataset, named “Relative Human” (RH), that contains weak annotations of *depth layers* and human ages categorized into the groups adult, teenager, child, and infant. Moreover, we propose a weakly supervised training scheme (WST) to effectively learn from these weak supervision signals. For instance, we use a piece-wise loss function that exploits the depth layers to penalize incorrect relative depth orders. Exploiting age information to constrain height is tricky. While age and height are correlated, heights can vary significantly within the same age group. Consequently, we develop an ambiguity-compatible mixed loss function that encourages body shapes with heights that lie within an ap-

appropriate range for each age group.

We evaluate BEV on two multi-person datasets: in-the-wild using the 2D RH and in 3D using the synthetic AGORA [24] dataset. On RH, compared with previous methods [10, 21, 34, 41], BEV is more accurate in relative depth reasoning and pose estimation. On AGORA, BEV significantly improves detection and achieves state-of-the-art results on “AGORA kids” in terms of the mesh reconstruction error. Also, fine-tuning on RH in a weakly supervised manner significantly improves the results for all age groups, especially for young people.

In summary, the main contributions are: (1) We construct a 3D representation to alleviate the monocular depth ambiguity via combining a front-view representation with a bird’s eye view. (2) We collect the Relative Human dataset with weak annotations of in-the-wild images, which facilitates the training and evaluation on monocular depth reasoning in multi-person scenes. (3) We develop a weakly supervised training scheme to learn from weak depth annotations and to exploit age information. Finally, code and data will be made available for research purposes.

## 2. Related Work

### Monocular 3D mesh regression from natural scenes.

Unlike many methods for 3D pose estimation that estimate the skeleton only, here we focus on regressing a 3D body mesh using a parametric model like SMPL [19] from a single RGB image. Most methods can be divided into multi-stage or single-stage approaches. For general multi-person cases, most existing methods [3, 5, 13, 16, 22, 25, 26] are based on a typical two-stage framework, which first detects people and then estimates the parameters of each person separately. Recent methods focus on exploring various supervision/refinement signals, such as temporal coherence [14], contour alignment [6], self-contact [23], or ground constraints [29] to enhance the geometric/dynamic consistency. However, for depth reasoning about all people in the scene, these multi-stage methods are not ideal. The processing of individual cropped people cannot exploit the scene context or reason about depth ordering.

A few one-stage methods [30, 39] estimate multiple 3D people simultaneously. Given a single image, ROMP outputs [30] a 2D Body Center Heatmap, Camera Map, and Parameter Map for 2D human detection, positioning, and mesh parameter regression, respectively. At the position parsed from the 2D Body Center heatmap, ROMP samples the final mesh parameters from the Camera and Parameter maps. These one-stage methods enjoy a holistic view of the image, which is more suitable for depth reasoning. However, they are based on 2D representations, like the 2D Body Center heatmap [30] or discretized multi-scale 2D center maps [39]. Like most methods, they model adults (with SMPL), train on images of adults, and therefore only pre-

dict adults. To tackle the limitations of their 2D representation and age bias, we propose BEV and its training scheme of learning age priors that constrain body height.

**Monocular depth reasoning.** Most previous methods for monocular 3D human mesh regression estimate bodies without depth reasoning. They place bodies in depth via post-processing. Due to their weak-perspective assumption and lack of prior information about the height of different age groups, depth relation of their results are unsatisfying. A few learning-based methods, like 3DMPPE [21] and CRMH [10], have made some attempts on depth reasoning. 3DMPPE is a detection-based, multi-stage, method for 3D pose estimation. They first compute an initial depth value based on the size of the bounding box and then estimate a correction factor from the image feature to derive the final depth result. CRMH takes advantage of instance segmentation to help the model learn the relative depth ordering of overlapping people. However, instance segmentation is expensive and CRMH has difficulty in learning depth relations from natural cases without overlapping people. SMAP [41] and HMOR [34] estimate a 2D depth map that represents the root depth of 3D pose at each pixel. However, these methods have problems with crowded scenes where the 2D representations are ambiguous. In contrast, BEV adopts a novel bird’s-eye-view-based 3D representation to distinguish people at different depths, therefore, it is more robust to the overlapping cases. Besides, for pair-wise depth reasoning, previous methods [4, 27, 34, 39] employ the same ordinal depth loss function. Nonetheless, we observe that it immoderately enlarges the depth difference between subjects of different depths, which leads to unreasonable depth predictions. Therefore, we develop a novel loss function to produce a reasonable penalty.

There are also multi-stage methods that exploit 3D joints and limbs as an intermediate representation. Zanfir et al. [36] take a bottom-up, part-based, grouping approach similar to [28]. In [35], they go further to take bottom-up 3D skeletons and constrain the transformation into SMPL bodies using ground-contact and interpenetration constraints. Instead of using either intermediate part or skeleton representation, BEV directly regresses to 3D body parameters. Most recently, Ugrinovic et al. [32] propose a multi-stage optimization-based method to optimize the 3D translation and scales of body meshes estimated by CRMH. Via an iterative optimization process, they enforce all predicted meshes to have their feet on the ground and then minimize the difference between the 2D projection of body joints and 2D pose estimations. In contrast, our learning-based, one-stage, framework is much more efficient. In addition, without feet-to-ground constraints, our method can adapt to more scenarios, like jumping.

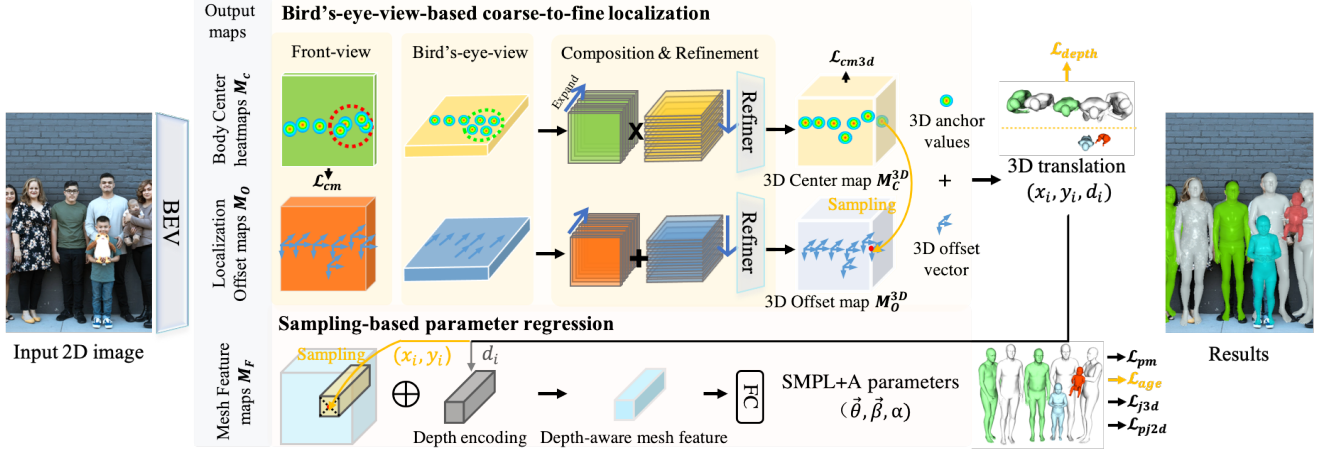


Figure 2. An overview of BEV. Given an RGB image, BEV performs the bird’s-eye-view-based coarse detection and fine localization to estimate the 3D translation of all people in the scene. Then via sampling-based parameter regression, we exploit the depth-aware feature to finally regress age-aware SMPL+A parameters of multiple people. See Sec. 3.1 for instructions.

### 3. Method

#### 3.1. Overview

The overall framework is illustrated in Fig. 2. BEV adopts a multi-head architecture. Given a single RGB image as input, BEV outputs 5 maps. For coarse-to-fine localization, we use the first 4 maps, which are the Body Center heatmaps and the Localization Offset maps in the front view and bird’s-eye view. We first expand the front-/bird’s-eye-view maps in depth/height wise and then combine them to generate the 3D Center/Offset maps. For coarse detection, we extract the rough 3D position of people from the 3D Center map. For fine localization, we sample the offset vectors from the 3D Offset map at the corresponding 3D center position. Adding these gives the 3D translation prediction. For 3D mesh parameter regression, we use the estimated 3D translation  $(x_i, y_i, d_i)$  and the Mesh Feature map. The depth value  $d_i$  of 3D translation is mapped to a depth encoding. At  $(x_i, y_i)$ , we sample a feature vector from the Mesh Feature map and add it with the depth encoding for final parameter regression. Finally, we convert the estimated parameters to body meshes using the SMPL+A model.

#### 3.2. SMPL+A: Mesh Representation for All Ages

The SMPL [19] and SMIL [8] models are developed to parameterize 3D body meshes of adults and infants into low-dimensional parameters. Recently, AGORA [24] further extends SMPL to support children by linearly blending the SMIL and SMPL template shapes with a weight  $\alpha \in [0, 1]$ , which we refer to as an “age offset.” While blending the templates to address scale and proportion differences between adults and children, AGORA uses the adult shape regardless of age. Additionally, AGORA does not address the representation of infants. We make a small, but important, change to better support all ages.

Following the notation of SMPL [19], the SMPL+A model defines a piece-wise function  $\vec{B} = \mathcal{M}(\vec{\theta}, \vec{\beta}, \alpha)$  that maps 3D pose  $\vec{\theta}$ , shape  $\vec{\beta}$ , and age offset  $\alpha$  to a 3D body mesh  $\vec{B} \in \mathbb{R}^{6890 \times 3}$ . Regarding the pose parameters  $\vec{\theta} \in \mathbb{R}^{6 \times 22}$ , we employ the first 22 body joints of SMPL and represent their 3D rotations in a 6D manner [42]. The shape parameter  $\vec{\beta} \in \mathbb{R}^{10}$  is the top-10 PCA coefficients of the mixed shape space.

The adult shape space of AGORA does not work for infants and results in unsatisfactory wrinkles on the mesh surface. Therefore, we still use SMIL for infants when the age offset  $\alpha$  is above a threshold  $t_\alpha$ . When  $\alpha > t_\alpha$ ,  $\mathcal{M}(\vec{\theta}, \vec{\beta}, \alpha)$  is the SMIL model  $\mathcal{M}_I(\vec{\theta}, \vec{\beta})$ . When the age offset  $\alpha \leq t_\alpha$ , we use the AGORA formulation

$$\mathcal{M}(\vec{\theta}, \vec{\beta}, \alpha) = W(T_A(\vec{\theta}, \vec{\beta}, \alpha; \bar{T}, \bar{T}_I), J(\vec{\beta}), \vec{\theta}, \mathcal{W}), \quad (1)$$

$$T_A(\cdot) = (1 - \alpha)\bar{T} + \alpha\bar{T}_I + B_S(\vec{\beta}) + B_P(\vec{\theta}),$$

which performs linear blend-skinning  $W(\cdot)$  with weights  $\mathcal{W}$ . In this process, it converts the T-posed mesh  $T_A(\cdot)$  to the target pose  $\vec{\theta}$  based on the skeleton joints  $J(\cdot)$ . The T-posed mesh  $T_A(\cdot)$  is the weighted sum of the templates  $(\bar{T}, \bar{T}_I)$ , shape-dependent deformation  $B_S(\cdot)$ , and pose-dependent deformation  $B_P(\cdot)$ . The age offset  $\alpha \in [0, 1]$  is used to interpolate between the adult SMPL template  $\bar{T}$  and the infant SMIL template  $\bar{T}_I$ . The larger the  $\alpha$ , the lower the mesh template height.

The 3D joints  $\vec{J}$  of the output mesh are derived via  $\mathcal{J}\vec{B}$ , where  $\mathcal{J} \in \mathbb{R}^{K \times 6890}$  is a sparse weight matrix that linearly maps the vertices  $\vec{B}$  to the  $K$  body joints. To supervise 3D joints  $\vec{J}$  with 2D keypoints, regression methods [13, 30] typically adopt a weak-perspective camera model to project  $\vec{J}$  into the image plane. For better depth reasoning, we employ a perspective camera model to perform projection; see SuppMat for the details of our camera model.

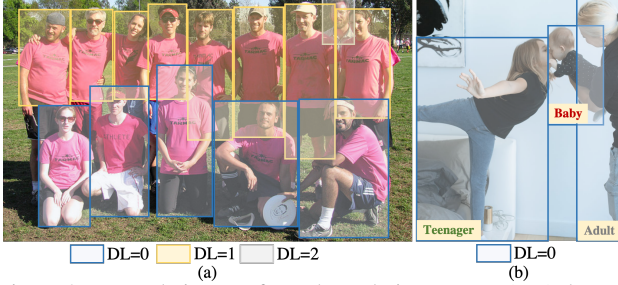


Figure 3. Example images from the Relative Human (RH) dataset with weak annotations: depth layers (DLs) and age group classification. Examples are a) adults at different DLs, and b) people of different age groups at the same DL.

### 3.3. Relative Human dataset

Existing in-the-wild datasets lack groups of overlapping people with annotations. Since acquiring 3D annotations of large crowds is challenging, we exploit more cost-effective weak annotations. We collect a new dataset, named Relative Human (RH), to support in-the-wild monocular human depth reasoning.

The images are collected from multiple sources to ensure diversity in age, ethnicity, gender, and scene. Most images are collected from the existing 2D pose datasets [17, 18, 40]. They contain few infants so we collect additional open-source family photos from Pexels [1] and then annotate their 2D poses. As shown in Fig. 3, we annotate the relative depth relationship between all people in the image. We treat subjects whose depth difference is less than one body-width ( $\gamma = 0.3m$ ) as people in the same layer. We then classify all people into different depth layers (DLs). Unlike prior work, which labels the ordinal relationships between pairs of joints of individuals [4], DLs capture the depth order of multiple people. Additionally, we label people with four age categories: adults, teenagers, children, and babies.

In total, we collect about 7.6K images with weak annotations of over 24.8K people. More than 21% of the subjects are young people (5.3K), including teenagers, children, and babies. For more analysis, please refer to SuppMat.

### 3.4. Representations

Figure 2 gives an overview of BEV’s representations.

**Heatmaps:** We build on the body-center heatmap representation from ROMP [30]. The front-view heatmap of size  $\mathbb{R}^{1 \times H \times W}$  is aligned with the pixel space and represents the likelihood of a body being centered at a 2D location using Gaussian kernels. We go beyond ROMP to add a second 2D heatmap of size  $\mathbb{R}^{1 \times D \times W}$  that represents an *unseen* bird’s-eye-view. This heatmap represents the likelihood of a person being at some point in depth; this map, however, does not represent metric depth. BEV composes and refines these two maps into a 3D heatmap,  $M_C^{3D} \in \mathbb{R}^{1 \times D \times H \times W}$ , which

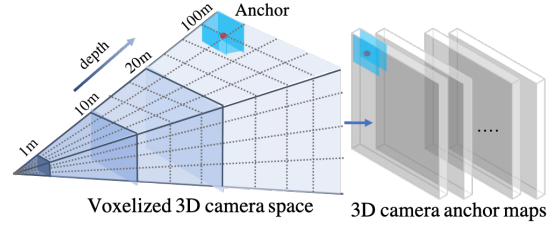


Figure 4. Pre-defined 3D camera anchor maps.

represents the 3D position of the detected human body centers with 3D Gaussian kernels.

**Offset maps:** The discretized center maps coarsely localize the body but we want the network to produce more precise estimates. To that end, we use additional maps that, at each position, add an estimated offset vector to refine the coarse detection. The front-view offset map of size  $\mathbb{R}^{3 \times H \times W}$  contains 3D offset vectors. The bird’s-eye-view offset map of size  $\mathbb{R}^{1 \times D \times W}$  contains 1D offset vectors for depth-wise correction.  $M_O^{3D} \in \mathbb{R}^{3 \times D \times H \times W}$  corresponds to the 3D centermap and contains a 3D offset vector at each 3D position.

**3D camera anchor maps:** The 3D center heatmap is defined in an arbitrary space, but to reason about people in the world, we transform it into a camera coordinate system called the anchor map. The anchor map is effectively a pre-defined transformation from the 3D centermap to a discrete, voxelized, world representation from the camera view. As shown in Fig. 4, we voxelize 3D camera space and each voxel center corresponds to a vector  $(x, y, d)$  representing its position in space; these are the anchor values. For convenience, we represent this as a set of maps with each map corresponding to a depth plane in discrete camera space. The 3D center heatmap is sampled to determine whether a person exists at each anchor position and the corresponding anchor values become its coarse location.

**Mesh feature map:**  $M_F \in \mathbb{R}^{128 \times H \times W}$  contains a 128-D mesh feature vector at each 2D position. These features are aligned with the input 2D image at the pixel level. After a 3D-center-based sampling process, the relevant features are used for the regression of SMPL+A parameters.

### 3.5. BEV

We now present the details of how the above representations work in our framework. To effectively establish the 3D representation, the front-view and the bird’s-eye-view must work together to estimate the image position and depth of corresponding subjects. Independently estimating the map of two views in parallel would inevitably cause misalignment, leading to the failure of 3D heatmap-based detection. To connect the two views, we estimate the bird’s-eye-view maps conditioned on the front-view maps. Specifically, to estimate the bird’s-eye-view map, we take the concatenation

tion of the front-view maps and the backbone feature maps as input. In this way, BEV focuses on the targets indicated by the front-view to estimate their depth. Then we expand and composite 2D maps of two views to generate 3D maps. To integrate 2D features from two views and enhance 3D consistency, we further perform 3D convolution on the composited 3D maps for refinement.

Next, we extract the 3D translation from the estimated 3D maps,  $M_C^{3D}, M_O^{3D}$ . High-confidence 3D positions of the 3D Center map are where we sample 3D offset vectors from the 3D Offset map. From the same 3D position in the 3D camera anchor maps (Fig. 4), we obtain the 3D anchor values, which are positions in camera space of the corresponding 3D center voxel. Adding the 3D offset vectors to the 3D anchor values gives the 3D translation as output.

Finally, we take the estimated 3D translation  $(x_i, y_i, d_i)$  and Mesh Feature maps  $M_F$  for parameter regression. We sample the pixel-level mesh feature vectors at  $(x_i, y_i)$  of  $M_F$ . Inspired by positional embeddings [33], we learn an embedding space to differentiate people at different depths, especially for the overlapping cases. The predicted depth value  $d_i$  is mapped to a 128-dim encoding vector via an embedding layer. Taking the sum of the depth encodings and the mesh feature vectors as input, we estimate the SMPL+A parameters  $(\vec{\theta}, \vec{\beta}, \alpha)$  via a fully-connected block. The output body meshes are obtained via Equation 1.

### 3.6. Loss Functions

Our loss functions are divided into two groups illustrated in Fig. 2: relative losses (in gold) and the standard mesh losses (in black). BEV is supervised by the weighted sum of all loss items. First, we introduce two relative loss functions for weakly supervised training (WST).

**Piece-wise depth layer loss  $\mathcal{L}_{depth}$ .**  $\mathcal{L}_{depth}$  is designed to supervise the predicted depth  $d_i, d_j$  of subject  $i, j$  by their depth layers  $r_i, r_j$  via

$$\begin{cases} (d_i - d_j)^2, & r_i = r_j \\ \log(1 + e^{d_i - d_j}) \prod((d_i - d_j) - \gamma(r_i - r_j)), & r_i < r_j \\ \log(1 + e^{d_j - d_i}) \prod(\gamma(r_i - r_j) - (d_i - d_j)), & r_i > r_j, \end{cases} \quad (2)$$

where  $\prod$  is a binarization function that maps positive values to 1 and negative values to 0.  $\prod$  is used to judge whether the BEV prediction is consistent with the depth relationship of the ground truth DLs.  $\mathcal{L}_{depth}$  is 0, if the predicted depth is difference within an acceptable range; that is, greater than the product of the DL difference and body-width  $\gamma$ . Otherwise,  $\mathcal{L}_{depth}$  will encourage the model to achieve it.

Previous ordinal depth losses [4, 27] encourage the model to enlarge the depth difference between people at different depth layers as much as possible. In contrast, the penalty in  $\mathcal{L}_{depth}$  is controlled within a range. This helps to avoid pushing remote subjects too far away.

**Ambiguity-compatible age loss  $\mathcal{L}_{age}$ .** The classification of age categories (infant, child, teenager, adult) is inherently ambiguous, especially for teenagers and children. Also, while height is correlated with age, one can easily find children who are taller than some adults. Consequently, we formulate an ambiguity-compatible mixed loss  $\mathcal{L}_{age}$ .

Rather than supervise height directly, we supervise the  $\alpha$  parameter that controls the blending between the SMIL infant body and the SMPL adult body. To do so, we define ranges of  $\alpha$  values for each age group; i.e. (lower-bound, middle, upper-bound). We do this using the statistical data of heights for each age category that we then relate these to ranges of  $\alpha$  values. Formally, the ranges are  $(\alpha_l^k, \alpha_m^k, \alpha_u^k), k = 1 \dots 4$  where  $k$  is the annotated age class number; see Sec. 4 for details.

BEV is then trained to predict the body shape as well as an  $\alpha$  value for each person. Given the predicted  $\alpha$  and ground truth age class  $k_g$ , the loss  $\mathcal{L}_{age}$  is defined as

$$\mathcal{L}_{age}(\alpha) = \begin{cases} 0, & \alpha_l^{k_g} < \alpha \leq \alpha_u^{k_g} \\ (\alpha - \alpha_m^{k_g})^2, & \text{otherwise.} \end{cases} \quad (3)$$

**Other losses.** Following the previous methods [13, 30], we employ the standard mesh losses to supervise the output maps and regressed SMPL+A parameters.  $\mathcal{L}_{cm}$  is the focal loss [30] of the front-view Body Center heatmap. In the same pattern, we further use a 3D focal loss  $\mathcal{L}_{cm3D}$  to supervise the 3D Center map via converting  $\mathcal{L}_{cm}$ 's 2D operation to 3D.  $\mathcal{L}_{pm}$  consists of three parts,  $\mathcal{L}_{\theta}, \mathcal{L}_{\beta}$ , and  $\mathcal{L}_{prior}$ .  $\mathcal{L}_{\theta}$  and  $\mathcal{L}_{\beta}$  are  $L_2$  loss of SMPL+A pose  $\vec{\theta}$ , shape  $\vec{\beta}$  parameters respectively.  $\mathcal{L}_{prior}$  is the Mixture of Gaussian pose prior [3, 19] on  $\vec{\theta}$ . To supervise the 3D body joints  $\vec{J}$ , we use  $\mathcal{L}_{j3d}$ , which is composed of  $\mathcal{L}_{mpj}$  and  $\mathcal{L}_{pmpj}$ .  $\mathcal{L}_{mpj}$  is the  $L_2$  loss of 3D joints  $\vec{J}$ . To alleviate the domain gap between training datasets, we follow [30, 31] to calculate the  $L_2$  loss  $\mathcal{L}_{pmpj}$  of the predicted 3D joints after Procrustes alignment with the ground truth.  $\mathcal{L}_{pj2d}$  is the  $L_2$  loss of the 2D projection of 3D joints  $\vec{J}$ . Lastly,  $w_{(\cdot)}$  denotes the corresponding weight of these losses.

## 4. Experiments

### 4.1. Implementation Details

**Training details.** For basic training, we use two 3D pose datasets (Human3.6M [9] and MuCo-3DHP [20]) and four 2D pose datasets (COCO [18], MPII [2], LSP [11], and CrowdPose [17]). We also use the pseudo SMPL annotations from [12] and WST on RH. Most samples in RH are collected from 2D pose datasets [17, 18, 40]. For a fair comparison, we only use the samples that are also used for training in compared methods [10, 15, 16, 21, 30, 41]. To compare with [15, 24], we further fine-tune our model and ROMP [30] on AGORA. The threshold for the age offset

| Method                        | Validation               |              |              |              |              | mPCK <sub>h</sub> <sup>0.6</sup> ↑ | Test                     |              |              |              |              | mPCK <sub>h</sub> <sup>0.6</sup> ↑ |
|-------------------------------|--------------------------|--------------|--------------|--------------|--------------|------------------------------------|--------------------------|--------------|--------------|--------------|--------------|------------------------------------|
|                               | PCDR <sup>0.2</sup> (%)↑ |              |              |              |              |                                    | PCDR <sup>0.2</sup> (%)↑ |              |              |              |              |                                    |
|                               | Baby                     | Kid          | Teen         | Adult        | All          |                                    | Baby                     | Kid          | Teen         | Adult        | All          |                                    |
| 3DMPPE <sup>†</sup> [21]      | 56.03                    | 59.51        | 70.49        | 59.64        | 60.16        | -                                  | 42.93                    | 54.66        | 61.44        | 59.07        | 58.85        | -                                  |
| CRMH [10]                     | 39.52                    | 54.62        | 60.16        | 57.36        | 57.68        | 0.793                              | 37.20                    | 48.41        | 62.28        | 58.58        | 58.44        | 0.806                              |
| SMAP [41]                     | 57.78                    | 55.17        | 34.55        | 39.72        | 40.91        | -                                  | 34.10                    | 44.39        | 48.06        | 41.49        | 42.15        | -                                  |
| ROMP [30]                     | 40.28                    | 52.43        | 67.69        | 59.17        | 59.96        | 0.874                              | 31.68                    | 48.03        | 56.11        | 58.79        | 58.86        | 0.880                              |
| BEV w/o WST                   | 41.27                    | 63.24        | 77.12        | 61.61        | 62.94        | 0.906                              | 37.94                    | 52.72        | 58.72        | 61.72        | 61.90        | <b>0.899</b>                       |
| BEV w/o $\mathcal{L}_{depth}$ | 61.48                    | 72.65        | 71.68        | 67.35        | 67.51        | 0.883                              | 46.33                    | 55.60        | 57.49        | 60.69        | 60.55        | 0.859                              |
| BEV w/o $\mathcal{L}_{age}$   | 79.02                    | <b>87.76</b> | 80.36        | 80.08        | 80.55        | 0.895                              | 48.72                    | 58.85        | 64.58        | 65.56        | 65.51        | 0.879                              |
| BEV                           | <b>80.77</b>             | 86.53        | <b>87.93</b> | <b>81.67</b> | <b>81.88</b> | <b>0.910</b>                       | <b>57.96</b>             | <b>61.60</b> | <b>64.82</b> | <b>66.86</b> | <b>66.61</b> | 0.894                              |

Table 1. Accuracy of relative depth relations (PCDR<sup>0.2</sup>) and projected 2D poses (mPCK<sub>h</sub><sup>0.6</sup>) on RH. We use official implementations of these papers to obtain results on RH. <sup>†</sup> uses the ground truth bounding boxes. BEV uses the same training samples as [30] to perform WST.

| Method      | Kid subset  |             |             |              |              |              | Full set     |             |             |             |              |              |              |              |
|-------------|-------------|-------------|-------------|--------------|--------------|--------------|--------------|-------------|-------------|-------------|--------------|--------------|--------------|--------------|
|             | Detection↑  |             |             | Matched↓     |              | All↓         |              | Detection↑  |             |             | Matched↓     |              | All↓         |              |
|             | F1 score    | Precision   | Recall      | MVE          | MPJPE        | NMVE         | NMJE         | F1 score    | Precision   | Recall      | MVE          | MPJPE        | NMVE         | NMJE         |
| SPIN [24]   | 0.31        | 0.21        | 0.60        | 186.7        | 191.7        | 602.3        | 618.4        | 0.77        | 0.91        | 0.67        | 148.9        | 153.4        | 193.4        | 199.2        |
| SPEC [15]   | 0.52        | 0.40        | 0.73        | 163.2        | 171.0        | 313.8        | 328.8        | 0.84        | 0.96        | 0.74        | 106.5        | 112.3        | 126.8        | 133.7        |
| ROMP [30]   | 0.50        | 0.37        | 0.80        | 156.6        | 159.8        | 313.2        | 319.6        | 0.91        | 0.95        | 0.88        | <b>103.4</b> | <b>108.1</b> | 113.6        | 118.8        |
| BEV w/o WST | <b>0.58</b> | <b>0.44</b> | <b>0.86</b> | 146.0        | 148.3        | 251.7        | 255.7        | 0.93        | 0.96        | 0.90        | 105.6        | 109.7        | 113.5        | 118.0        |
| BEV         | 0.56        | 0.42        | 0.85        | <b>129.1</b> | <b>132.1</b> | <b>230.5</b> | <b>235.9</b> | <b>0.93</b> | <b>0.96</b> | <b>0.90</b> | 104.6        | 108.9        | <b>112.5</b> | <b>117.1</b> |

Table 2. Comparison of SOTA methods on AGORA test set. All methods are fine-tuned on the AGORA training set or synthetic data [15] generated in the same way as AGORA. We fine-tune ROMP [30] using the public implementation; results from the AGORA leaderboard.

is set to  $t_\alpha = 0.8$ . The age offset ranges ( $\alpha_l^k, \alpha_m^k, \alpha_u^k$ ) are: adults  $(-0.05, 0, 0.15)$ , teenagers  $(0.15, 0.3, 0.45)$ , children  $(0.45, 0.6, 0.75)$ , and infants  $(0.75, 0.9, 1)$ . See Sup. Mat. for more details.

**Evaluation benchmarks.** We evaluate BEV on two multi-person datasets, RH and AGORA [24], containing 257 child scans and significant person-person occlusion.

**Evaluation matrix.** To evaluate the accuracy of depth reasoning, we employ the Percentage of Correct Depth Relations (PCDR<sup>0.2</sup>), and set the threshold for equal depth to  $0.2m$ . To evaluate the accuracy of projected 2D poses on RH, we also report the mean Percentage of Correct Key-points (mPCK<sub>h</sub><sup>0.6</sup>), setting the matching threshold to 0.6 times the head length.

Also, following AGORA [24], we evaluate the accuracy of 3D pose/mesh estimation while considering missing detections. To evaluate the detection accuracy, we report **Precision**, **Recall**, and **F1 score**. For matched detections, we report the Mean Per Joint Position Error (MPJPE) and Mean Vertex Error (MVE). To punish misses and false alarms in detection, we normalize the MPJPE and MVE by F1 score to get Normalized Mean Joint Error (NMJE) and Normalized Mean Vertex Error (NMVE).

## 4.2. Comparisons to the state-of-the-art methods

**Monocular depth reasoning.** We first evaluate BEV on monocular depth reasoning in Tab. 1 using the RH dataset. We first compare with the most competitive methods [10, 21, 41], which solve depth relations in monocular images. We also compare with ROMP [30], for one-stage multi-person

mesh recovery. Their 3D translation results are obtained by solving the PnP algorithm (RANSAC [7]) between their 3D pose and projected 2D pose predictions. As shown in Tab. 1, BEV outperforms all these methods in the accuracy of both depth reasoning and projected 2D poses by a large margin.

**Monocular detection and mesh regression.** We also run BEV on AGORA to evaluate the detection and 3D mesh accuracy. We compare with the state-of-the-art (SOTA) multi-stage methods [15, 24] and the one-stage ROMP [30]. Tab. 2 shows that BEV outperforms SOTA methods on detection by 10.7% and 2.1% in terms of F1 score on the kid and full subset, respectively. Tab. 3 shows that BEV’s advantage is even greater (5.6%) under severe occlusion (over 70%). This is evidence that the 3D representation helps alleviate depth ambiguity in crowded scenes. On the kid subset, BEV also significantly outperforms all existing methods on the leaderboard in terms of mesh reconstruction. Especially, compared with ROMP [30], BEV reduces errors over 17% and 26% in terms of matched MVE and all NMVE, indicating that BEV effectively reduces the age bias using WST.

## 4.3. Ablation Studies

**Bird’s-eye-view representation & BEV w/o WST.** To further verify the effectiveness of BEV’s 3D representation, we train it without performing WST on RH and compare it with SOTA methods on AGORA and RH. On RH in Tab. 1, compared with 3DMPPE [21], which uses the ground truth bounding boxes to assist the prediction, the depth reasoning accuracy of BEV w/o WST is 4.4% higher (PCDR<sup>0.2</sup> of all). BEV w/o WST also outperforms the



Figure 5. Qualitative results on AGORA, RH, and Internet images [1]. Note how children and adults are properly placed in depth.

2D representation-based network ROMP [30]. These results point to the effectiveness of our 3D representation for dealing with monocular depth ambiguity. On AGORA, as shown in Tab. 2, BEV w/o WST significantly outperforms ROMP in all detection metrics. Additionally, the strong detection ability of the 3D representation makes BEV w/o WST outperform the SOTA methods [15, 24, 30] in terms of NMVE and NMJE. Comparing BEV and BEV w/o WST in Tab. 3 also shows that our gains in high occlusion situations come from the 3D representation.

**Weakly supervised training (WST) losses,  $\mathcal{L}_{depth}$  and  $\mathcal{L}_{age}$ .** Results on AGORA and RH in Tab. 1 and 2 show that performing WST significantly improves the performance, especially for the young groups. Also, Tab. 1 shows that separately using  $\mathcal{L}_{depth}$  or  $\mathcal{L}_{age}$  make BEV produce better depth reasoning than BEV w/o WST, and using both terms will make BEV perform best.

**Depth encoding (DC) for 3D mesh parameter regression.** Tab. 3 shows that adding the depth encoding reduces mesh reconstruction error under high occlusion (over 70%).

**Piece-wise depth layer loss  $\mathcal{L}_{depth}$  v.s. ordinal depth loss [34, 39].** Different from the ordinal depth loss, our  $\mathcal{L}_{depth}$  keeps the penalty into a reasonable range (see Sec. 3.6). As shown in Tab. 4, training with the proposed  $\mathcal{L}_{depth}$  instead of the ordinal depth loss significantly reduces the 3D translation error on the validation set of AGORA, especially in depth.

## 5. Conclusion, Limitations, Ethics, Risks

In this paper, we introduce BEV, a unified one-stage method for monocular regression and depth reasoning of multiple 3D people. By introducing a novel bird’s eye view representation, we enable powerful 3D reasoning that reduces the monocular depth ambiguity. Exploiting the correlation between body height and depth, BEV learns depth reasoning from complex in-the-wild scenes by exploiting

| Method    | F1 score $\uparrow$ | MVE $\downarrow$ | MPJPE $\downarrow$ | NMVE $\downarrow$ | NMJE $\downarrow$ |
|-----------|---------------------|------------------|--------------------|-------------------|-------------------|
| ROMP [30] | 0.695               | 173.76           | 170.55             | 249.96            | 245.34            |
| BEV       | <b>0.737</b>        | <b>168.52</b>    | <b>164.69</b>      | <b>228.39</b>     | <b>223.20</b>     |
| w/o WST   | 0.738               | 171.16           | 168.12             | 235.06            | 230.89            |
| w/o DC    | 0.741               | 170.59           | 168.12             | 229.98            | 225.67            |

Table 3. 3D mesh/pose error on AGORA-PC, the high occlusion (over 70%) subset of the AGORA validation set (no kids). This has ground truth 3D annotations for detailed evaluation while the test set does not. BEV uses the same training samples as [30].

| Method                                  | Dist. $\downarrow$ | X $\downarrow$ | Y $\downarrow$ | Depth $\downarrow$ |
|---|--------------------|----------------|----------------|--------------------|
| Ordinal loss [34, 39]                   | 0.608              | 0.153          | 0.184          | 0.509              |
| Piece-wise $\mathcal{L}_{depth}$ (ours) | <b>0.463</b>       | <b>0.121</b>   | <b>0.160</b>   | <b>0.374</b>       |

Table 4. 3D translation error on AGORA validation set.

relative depth relations and age group classification. We make available an in-the-wild dataset to promote the training and evaluation of monocular depth reasoning in the wild. The ablation studies point to the value of the 3D representation and depth encoding in the network, the importance of our training scheme, and the value of the collected dataset. BEV is a preliminary attempt to explore complex multi-person relationships in the 3D world, and we hope the framework will serve as a simple yet effective foundation for future progress.

**Limitations.** There is much to do. While BEV goes beyond current methods to cover more diverse ages, it is not trained to capture diverse weights, gender, ethnicity, etc. Our labeling approach, however, suggests that weak labels can produce strong results; i.e. improved metric accuracy. Note that BEV is not trained or designed to deal with “crowds” (e.g. 100’s of people); this is future work.

**Ethics and data.** We collect images of RH from a free photo website [1] under a Creative Commons license that enables sharing. We strove to have a dataset that is diverse in age, ethnicity, and gender. Also, our weak annotations



do not contain any personal information and the annotators, themselves, are anonymous and were not studied.

**Potential Negative Societal Impacts.** Methods for monocular 3D pose and shape estimation might be used for automated surveillance, tracking, and behavior analysis, which may violate people’s privacy. To help prevent this, BEV will be released for research only.

**Disclosure:** MJB has received research funds from Adobe, Intel, Nvidia, Facebook, and Amazon. While MJB is a part-time employee of Amazon, his research was performed solely at Max Planck. MJB has financial interests in Amazon, Datagen Technologies, and Meshcapade GmbH.

## References

- [1] Pexels. <https://www.pexels.com>. 5, 8
- [2] Mykhaylo Andriluka, Leonid Pishchulin, Peter Gehler, and Bernt Schiele. 2D human pose estimation: New benchmark and state of the art analysis. In *CVPR*, pages 3686–3693, 2014. 6
- [3] Federica Bogo, Angjoo Kanazawa, Christoph Lassner, Peter Gehler, Javier Romero, and Michael J Black. Keep it SMPL: Automatic estimation of 3D human pose and shape from a single image. In *ECCV*, pages 561–578, 2016. 2, 3, 6
- [4] Weifeng Chen, Zhao Fu, Dawei Yang, and Jia Deng. Single-image depth perception in the wild. *NIPS*, pages 730–738, 2016. 3, 5, 6
- [5] Hongsuk Choi, Gyeongsik Moon, JoonKyu Park, and Kyoung Mu Lee. 3dcrowdnet: 2d human pose-guided 3d crowd human pose and shape estimation in the wild. *arXiv*, 2021. 3
- [6] Sai Kumar Dwivedi, Nikos Athanasiou, Muhammed Kocabas, and Michael J. Black. Learning to regress bodies from images using differentiable semantic rendering. In *ICCV*, pages 11250–11259, 2021. 3
- [7] Martin A Fischler and Robert C Bolles. Random sample consensus: a paradigm for model fitting with applications to image analysis and automated cartography. *Communications of the ACM*, pages 381–395, 1981. 7
- [8] Nikolas Hesse, Sergi Pujades, Javier Romero, Michael J Black, Christoph Bodensteiner, Michael Arens, Ulrich G Hofmann, Uta Tacke, Mijna Hadders-Algra, Raphael Weinberger, et al. Learning an infant body model from rgb-d data for accurate full body motion analysis. In *MICCAI*, pages 792–800, 2018. 4
- [9] Catalin Ionescu, Dragos Papava, Vlad Olaru, and Cristian Sminchisescu. Human3.6M: Large scale datasets and predictive methods for 3D human sensing in natural environments. *TPAMI*, pages 1325–1339, 2014. 6
- [10] Wen Jiang, Nikos Kolotouros, Georgios Pavlakos, Xiaowei Zhou, and Kostas Daniilidis. Coherent reconstruction of multiple humans from a single image. In *CVPR*, pages 5579–5588, 2020. 2, 3, 6, 7
- [11] Sam Johnson and Mark Everingham. Learning effective human pose estimation from inaccurate annotation. In *CVPR*, pages 1465–1472, 2011. 6
- [12] Hanbyul Joo, Natalia Neverova, and Andrea Vedaldi. Exemplar fine-tuning for 3D human pose fitting towards in-the-wild 3D human pose estimation. In *ECCV*, 2020. 6
- [13] Angjoo Kanazawa, Michael J. Black, David W. Jacobs, and Jitendra Malik. End-to-end recovery of human shape and pose. In *CVPR*, pages 7122–7131, 2018. 2, 3, 4, 6
- [14] Muhammed Kocabas, Nikos Athanasiou, and Michael J Black. VIBE: Video inference for human body pose and shape estimation. In *CVPR*, pages 5253–5263, 2020. 2, 3
- [15] Muhammed Kocabas, Chun-Hao P. Huang, Joachim Tesch, Lea Müller, Otmar Hilliges, and Michael J. Black. SPEC: Seeing people in the wild with an estimated camera. In *ICCV*, pages 11035–11045, 2021. 2, 6, 7, 8
- [16] Nikos Kolotouros, Georgios Pavlakos, Michael J Black, and Kostas Daniilidis. Learning to reconstruct 3D human pose and shape via model-fitting in the loop. In *ICCV*, pages 2252–2261, 2019. 2, 3, 6
- [17] Jiefeng Li, Can Wang, Hao Zhu, Yihuan Mao, Hao-Shu Fang, and Cewu Lu. CrowdPose: Efficient crowded scenes pose estimation and a new benchmark. In *CVPR*, pages 10863–10872, 2019. 5, 6
- [18] Tsung-Yi Lin, Michael Maire, Serge Belongie, James Hays, Pietro Perona, Deva Ramanan, Piotr Dollár, and C Lawrence Zitnick. Microsoft coco: Common objects in context. In *ECCV*, pages 740–755, 2014. 5, 6
- [19] Matthew Loper, Naureen Mahmood, Javier Romero, Gerard Pons-Moll, and Michael J. Black. SMPL: A skinned multi-person linear model. *TOG*, pages 1–16, 2015. 2, 3, 4, 6
- [20] Dushyant Mehta, Oleksandr Sotnychenko, Franziska Mueller, Weipeng Xu, Srinath Sridhar, Gerard Pons-Moll, and Christian Theobalt. Single-shot multi-person 3D pose estimation from monocular rgb. In *3DV*, pages 120–130, 2018. 6
- [21] Gyeongsik Moon, Ju Yong Chang, and Kyoung Mu Lee. Camera distance-aware top-down approach for 3D multi-person pose estimation from a single RGB image. In *CVPR*, pages 10133–10142, 2019. 2, 3, 6, 7
- [22] Gyeongsik Moon and Kyoung Mu Lee. Pose2pose: 3d positional pose-guided 3d rotational pose prediction for expressive 3d human pose and mesh estimation. *arXiv*, 2020. 2, 3
- [23] Lea Muller, Ahmed AA Osman, Siyu Tang, Chun-Hao P Huang, and Michael J Black. On self-contact and human pose. In *CVPR*, pages 9990–9999, 2021. 3
- [24] Priyanka Patel, Chun-Hao P Huang, Joachim Tesch, David T Hoffmann, Shashank Tripathi, and Michael J Black. Agora: Avatars in geography optimized for regression analysis. In *CVPR*, pages 13468–13478, 2021. 3, 4, 6, 7, 8
- [25] Georgios Pavlakos, Vasileios Choutas, Nima Ghorbani, Timo Bolkart, Ahmed AA Osman, Dimitrios Tzionas, and Michael J Black. Expressive body capture: 3d hands, face, and body from a single image. In *CVPR*, pages 10975–10985, 2019. 3
- [26] Georgios Pavlakos, Nikos Kolotouros, and Kostas Daniilidis. TexturePose: Supervising human mesh estimation with texture consistency. In *ICCV*, pages 803–812, 2019. 2, 3

- [27] Georgios Pavlakos, Xiaowei Zhou, and Kostas Daniilidis. Ordinal depth supervision for 3d human pose estimation. In *CVPR*, pages 7307–7316, 2018. [3](#), [6](#)
- [28] Leonid Pishchulin, Eldar Insafutdinov, Siyu Tang, Bjoern Andres, Mykhaylo Andriluka, Peter V Gehler, and Bernt Schiele. Deepcut: Joint subset partition and labeling for multi person pose estimation. In *CVPR*, pages 4929–4937, 2016. [3](#)
- [29] Davis Remppe, Tolga Birdal, Aaron Hertzmann, Jimei Yang, Srinath Sridhar, and Leonidas J. Guibas. Humor: 3d human motion model for robust pose estimation. In *ICCV*, pages 11488–11499, 2021. [3](#)
- [30] Yu Sun, Qian Bao, Wu Liu, Yili Fu, Michael J Black, and Tao Mei. Monocular, one-stage, regression of multiple 3d people. In *ICCV*, pages 11179–11188, 2021. [2](#), [3](#), [4](#), [5](#), [6](#), [7](#), [8](#)
- [31] Yu Sun, Yun Ye, Wu Liu, Wenpeng Gao, YiLi Fu, and Tao Mei. Human mesh recovery from monocular images via a skeleton-disentangled representation. In *ICCV*, pages 5348–5357, 2019. [2](#), [6](#)
- [32] Nicolas Ugrinovic, Adria Ruiz, Antonio Agudo, Alberto Sanfeliu, and Francesc Moreno-Noguer. Body size and depth disambiguation in multi-person reconstruction from single images. *3DV*, 2021. [3](#)
- [33] Ashish Vaswani, Noam Shazeer, Niki Parmar, Jakob Uszkoreit, Llion Jones, Aidan N Gomez, Łukasz Kaiser, and Illia Polosukhin. Attention is all you need. In *NeurIPS*, pages 5998–6008, 2017. [6](#)
- [34] Can Wang, Jiefeng Li, Wentao Liu, Chen Qian, and Cewu Lu. Hmor: Hierarchical multi-person ordinal relations for monocular multi-person 3d pose estimation. In *ECCV*, pages 242–259, 2020. [2](#), [3](#), [8](#)
- [35] Andrei Zanfir, Elisabeta Marinoiu, and Cristian Sminchisescu. Monocular 3D pose and shape estimation of multiple people in natural scenes—the importance of multiple scene constraints. In *CVPR*, pages 2148–2157, 2018. [3](#)
- [36] Andrei Zanfir, Elisabeta Marinoiu, Mihai Zanfir, Alin-Ionut Popa, and Cristian Sminchisescu. Deep network for the integrated 3D sensing of multiple people in natural images. In *NeurIPS*, pages 8410–8419, 2018. [3](#)
- [37] Wang Zeng, Wanli Ouyang, Ping Luo, Wentao Liu, and Xiaogang Wang. 3d human mesh regression with dense correspondence. In *CVPR*, pages 7054–7063, 2020. [2](#)
- [38] Hongwen Zhang, Yating Tian, Xinchu Zhou, Wanli Ouyang, Yebin Liu, Limin Wang, and Zhenan Sun. Pymaf: 3d human pose and shape regression with pyramidal mesh alignment feedback loop. In *ICCV*, pages 7054–7063, 2021. [2](#)
- [39] Jianfeng Zhang, Dongdong Yu, Jun Hao Liew, Xuecheng Nie, and Jiashi Feng. Body meshes as points. In *CVPR*, pages 546–556, 2021. [2](#), [3](#), [8](#)
- [40] Song-Hai Zhang, Ruilong Li, Xin Dong, Paul Rosin, Zixi Cai, Xi Han, Dingcheng Yang, Haozhi Huang, and Shi-Min Hu. Pose2seg: Detection free human instance segmentation. In *CVPR*, pages 889–898, 2019. [5](#), [6](#)
- [41] Jianan Zhen, Qi Fang, Jiaming Sun, Wentao Liu, Wei Jiang, Hujun Bao, and Xiaowei Zhou. SMAP: Single-shot multi-person absolute 3D pose estimation. In *ECCV*, pages 550–566, 2020. [2](#), [3](#), [6](#), [7](#)
- [42] Yi Zhou, Connelly Barnes, Lu Jingwan, Yang Jimei, and Li Hao. On the continuity of rotation representations in neural networks. In *CVPR*, pages 5745–5753, 2019. [4](#)